Research Article | Vol. 24, No. 22 | 31 Oct 2016 | OPTICS EXPRESS 25785

Optics EXPRESS

Hybrid cavity-coupled plasmonic biosensors for low concentration, label-free and selective biomolecular detection.

ABRAHAM VÁZQUEZ-GUARDADO,[1,2] ALEXANDRA SMITH,[2,3] WADE WILSON,[4] JEANETTE ORTEGA,[5] J. MANUEL PEREZ,[2,3,4] DEBASHIS CHANDA[1,2,4,6,*]

[1] *CREOL, The College of Optics and Photonics, University of Central Florida, Orlando, FL 32816, USA*
[2] *NanoScience Technology Center, University of Central Florida, Orlando, FL 32826, USA*
[3] *Department of Chemistry, University of Central Florida, Orlando, FL 32816, USA*
[4] *Department of Electrical & Computer Engineering, University of Central Florida, Orlando, FL 32816, USA*
[5] *Department of Material Science & Engineering, Johns Hopkins University, Baltimore, MD 21218, USA*
[6] *Department of Physics, University of Central Florida, Orlando, FL 32816, USA*
[*] *debashis.chanda@creol.ucf.edu*

Abstract: Simple optical techniques that can accurately and selectively identify organic and inorganic material in a reproducible manner are of paramount importance in biological sensing applications. In this work, we demonstrate that a nanoimprinted plasmonic pattern with locked-in dimensions supports sharp deterministic hybrid resonances when coupled with an optical cavity suitable for high sensitive surface detection. The surface sensing property of this hybrid system is quantified by precise atomic layer growth of aluminum oxide using the atomic layer deposition technique. The analyte specific sensing ability is demonstrated in the detection of two dissimilar analytes, inorganic amine-coated iron oxide nanoparticles and organic streptavidin protein. Femto to nanomolar detection limits were achieved with the proposed coupled plasmonic system based on the versatile and robust soft nanoimprinting technique, which promises practical low cost biosensors.

OCIS codes: (300.0300) Spectroscopy; (050.1950) Diffraction gratings; (280.1415) Biological sensing and sensors;(250.5403) Plasmonics; (310.6628) Subwavelength structures, nanostructures.

References and links

1. S. Loeb and W. J. Catalona, "What to do with an abnormal PSA test," Oncologist **13**, 299–305 (2008).
2. P. L. Mai, N. Wentzensen, and M. H. Greene, "Challenges related to developing serum-based biomarkers for early ovarian cancer detection," Cancer Prev. Res. **4**, 303–306 (2011).
3. A. V. Vlassov, S. Magdaleno, R. Setterquist, and R. Conrad, "Exosomes: current knowledge of their composition, biological functions, and diagnostic and therapeutic potentials," BBA - Gen. Subjects **1820**, 940–948 (2012).
4. P. Kharaziha, S. Ceder, Q. Li, and T. Panaretakis, "Tumor cell-derived exosomes: a message in a bottle," BBA-Rev. Cancer **1826**(1), 103–111 (2012).
5. G. W. Litman, J. P. Rast, M. J. Shamblott, R. N. Haire, M. Hulst, W. Roess, R. T. Litman, K. R. Hinds-Frey, A. Zilch, and C. T. Amemiya, "Phylogenetic diversification of immunoglobulin genes and the antibody repertoire," Mol. Biol. Evol. **10**(1), 60–72 (1993).
6. W. David, *The Immunoassay Handbook*, 3rd ed. (Elsevier, 2005).
7. J. Anker, W. Hall, O. Lyandres, N. Shah, J. Zhao, and R. Van Duyne, "Biosensing with plasmonic nanosensors," Nat. Mater. **7**(6), 442–453 (2008).
8. M. E. Stewart, C. R. Anderton, L. B. Thompson, J. Maria, S. K. Gray, J. A. Rogers, and R. G. Nuzzo, "Nanostructured plasmonic sensors," Chem. Rev. **108**(2), 494–521 (2008).
9. S. A. Maier and H. A. Atwater, "Plasmonics: localization and guiding of electromagnetic energy in metal/dielectric structures," J. Appl. Phys. **98**, 011101 (2005).
10. S. Chen, M. Svedendahl, M. Käll, L. Gunnarsson, and A. Dmitriev, "Ultrahigh sensitivity made simple: nanoplasmonic label-free biosensing with an extremely low limit-of-detection for bacterial and cancer diagnostics," Nanotechnology **20**(43), 434015 (2009).
11. S. Zhang, Y. Moustafa, and Q. Huo, "Different interaction modes of biomolecules with citrate-capped gold nanoparticles," ACS Appl. Mater. Inter. **6**(23), 21184–21192 (2014).

#273704 http://dx.doi.org/10.1364/OE.24.025785
Journal © 2016 Received 12 Aug 2016; revised 14 Oct 2016; accepted 18 Oct 2016; published 26 Oct 2016

Optics EXPRESS

12. H. Im, H. Shao, Y. Il Park, V. M. Peterson, C. M. Castro, R. Weissleder, and H. Lee, "Label-free detection and molecular profiling of exosomes with a nano-plasmonic sensor," Nat. Biotechnol. **32**(5), 490–495 (2014).
13. S. S. Aćimović, M. A. Ortega, V. Sanz, J. Berthelot, J. L. Garcia-Cordero, J. Renger, S. J. Maerkl, M. P. Kreuzer, and R. Quidant, "LSPR chip for parallel, rapid, and sensitive detection of cancer markers in serum," Nano Lett. **14**(5), 2636–2641 (2014).
14. S. Y. Hwang, C. H. Yoon, J. Y. Jeon, S. C. Choi, and E. K. Lee, "Quantitative assay of Hepatitis B surface antigen by using surface plasmon resonance biosensor," Biotechnol. Bioproc. E. **10**(4), 309–314 (2005).
15. J. W. Chung, S. D. Kim, R. Bernhardt, and J. C. Pyun, "Application of SPR biosensor for medical diagnostics of human Hepatitis B virus (hHBV)," Sensor Actuat. B-Chem. **111-112**, 416–422 (2005).
16. A. J. Haes, L. Chang, W. L. Klein, and R. P. Van Duyne, "Detection of a biomarker for Alzheimer's disease from synthetic and clinical samples using a nanoscale optical biosensor," J. Am. Chem. Soc. **127**(7), 2264–2271 (2005).
17. M. K. Kang, J. Lee, A. H. Nguyen, and S. J. Sim, "Label-free detection of ApoE4-mediated β-amyloid aggregation on single nanoparticle uncovering Alzheimer's disease," Biosens. Bioelectron. **72**, 197–204 (2015).
18. M. Mesch, C. Zhang, P. V. Braun, and H. Giessen, "Functionalized hydrogel on plasmonic nanoantennas for noninvasive glucose sensing," ACS Photonics **2**(4), 475–480 (2015).
19. C.-A. Peng and S. Pachpinde, "Longitudinal plasmonic detection of glucose using gold nanorods," Nanomater. Nanotechnol. **4**, 9 (2014).
20. X. Liu, S. Zhang, P. Tan, J. Zhou, Y. Huang, Z. Nie, and S. Yao, "A plasmonic blood glucose monitor based on enzymatic etching of gold nanorods," Chem. Commun. **49**(18), 1856 (2013).
21. Z. Altintas, Y. Uludag, Y. Gurbuz, and I. Tothill, "Development of surface chemistry for surface plasmon resonance based sensors for the detection of proteins and DNA molecules," Anal. Chim. Acta. **712**, 138–144 (2012).
22. M. Cottat, N. Thioune, A.-M. Gabudean, N. Lidgi-Guigui, M. Focsan, S. Astilean, and M. Lamy de la Chapelle, "Localized Surface Plasmon Resonance (LSPR) biosensor for the protein detection," Plasmonics **8**(2), 699–704 (2012).
23. J. Zhao, A. Das, X. Zhang, G. C. Schatz, S. G. Sligar, and R. P. Van Duyne, "Resonance surface plasmon spectroscopy: low molecular weight substrate binding to cytochrome P450," J. Am. Chem. Soc. **128**(34), 11004–11005 (2006).
24. L. Guo, J. A. Jackman, H.-H. Yang, P. Chen, N.-J. Cho, and D.-H. Kim, "Strategies for enhancing the sensitivity of plasmonic nanosensors," Nano Today **10**(2), 213–239 (2015).
25. V. G. Kravets, F. Schedin, R. Jalil, L. Britnell, R. V. Gorbachev, D. Ansell, B. Thackray, K. S. Novoselov, A. K. Geim, A. V. Kabashin, and A. N. Grigorenko, "Singular phase nano-optics in plasmonic metamaterials for label-free single-molecule detection," Nat. Mater. **12**(4), 304–309 (2013).
26. N. Liu, M. Mesch, T. Weiss, M. Hentschel, and H. Giessen, "Infrared perfect absorber and its application as plasmonic sensor," Nano Lett. **10**(7), 2342–2348 (2010).
27. S. Yokogawa, S. P. Burgos, and H. A. Atwater, "Plasmonic color filters for CMOS image sensor applications," Nano Lett. **12**(8), 4349–4354 (2012).
28. C. Escobedo, A. G. Brolo, R. Gordon, and D. Sinton, "Optofluidic concentration: plasmonic nanostructure as concentrator and sensor," Nano Lett. **12**(3), 1592–1596 (2012).
29. J. C. Hulteen and R. Van Duyne, "Nanosphere lithography: a materials general fabrication process for periodic particle array surfaces," J. Vac. Sci. Technol. A **13**(3), 1553 (1995).
30. H. Fredriksson, Y. Alaverdyan, A. Dmitriev, C. Langhammer, D. S. Sutherland, M. Zäch, and B. Kasemo, "Hole–mask colloidal lithography," Adv. Mater. **19**(23), 4297–4302 (2007).
31. A. Nemiroski, M. Gonidec, J. M. Fox, P. Jean-Remy, E. Turnage, and G. M. Whitesides, "Engineering shadows to fabricate optical metasurfaces," ACS Nano **8**(11), 11061–11070 (2014).
32. A. Cattoni, P. Ghenuche, A.-M. Haghiri-Gosnet, D. Decanini, J. Chen, J.-L. Pelouard, and S. Collin, "λ 3/1000 plasmonic nanocavities for biosensing fabricated by soft UV nanoimprint lithography," Nano Lett. **11**(9), 3557–3563 (2011).
33. K. Lodewijks, W. Van Roy, G. Borghs, L. Lagae, and P. Van Dorpe, "Boosting the figure-of-merit of LSPR-based refractive index sensing by phase-sensitive measurements," Nano Lett. **12**(3), 1655–1659 (2012).
34. A. Vázquez-Guardado, A. Safaei, S. Modak, D. Franklin, and D. Chanda, "Hybrid coupling mechanism in a system supporting high order diffraction, plasmonic, and cavity resonances," Phys. Rev. Lett. **113**(26), 263902 (2014).
35. D. Chanda, K. Shigeta, T. Truong, E. Lui, A. Mihi, M. Schulmerich, P. V. Braun, R. Bhargava, and J. A. Rogers, "Coupling of plasmonic and optical cavity modes in quasi-three-dimensional plasmonic crystals," Nat. Commun. **2**, 479 (2011).
36. A. E. Cetin and H. Altug, "Fano resonant ring/disk plasmonic nanocavities on conducting substrates for advanced biosensing," ACS Nano **6**(11), 9989–9995 (2012).
37. A. A. Yanik, A. E. Cetin, M. Huang, A. Artar, S. H. Mousavi, A. Khanikaev, J. H. Connor, G. Shvets, and H. Altug, "Seeing protein monolayers with naked eye through plasmonic Fano resonances," Proc. Natl. Acad. Sci. USA **108**(29), 11784–11789 (2011).
38. Y. Shen, J. Zhou, T. Liu, Y. Tao, R. Jiang, M. Liu, G. Xiao, J. Zhu, Z.-K. Zhou, X. Wang, C. Jin, and J. Wang, "Plasmonic gold mushroom arrays with refractive index sensing figures of merit approaching the theoretical limit," Nat. Commn. **4**, 2381 (2013).
39. R. Ameling, L. Langguth, M. Hentschel, M. Mesch, P. V. Braun, and H. Giessen, "Cavity-enhanced localized plasmon resonance sensing," Appl. Phys. Lett. **97**(25), 253116 (2010).

Optics EXPRESS

40. M. Bahramipanah, S. Dutta-Gupta, B. Abasahl, and O. J. F. Martin, "Cavity-coupled plasmonic device with enhanced sensitivity and figure-of-merit," ACS Nano **9**(7), 7621–7633 (2015).
41. J. Li, J. Ye, C. Chen, Y. Li, N. Verellen, V. V. Moshchalkov, L. Lagae, and P. Van Dorpe, "Revisiting the surface sensitivity of nanoplasmonic biosensors," ACS Photonics **2**(3), 425–431 (2015).
42. M. A. Otte, B. Sepúlveda, W. Ni, J. P. Juste, L. M. Liz-Marzán, and L. M. Lechuga, "Identification of the optimal spectral region for plasmonic and nanoplasmonic sensing," ACS Nano **4**(1), 349–357 (2010).
43. V. Malyarchuk, F. Hua, N. Mack, V. Velasquez, J. White, R. Nuzzo, and J. Rogers, "High performance plasmonic crystal sensor formed by soft nanoimprint lithography," Opt. Express **13**(15), 5669–5675 (2005).
44. M. E. Stewart, N. H. Mack, V. Malyarchuk, J. A. N. T. Soares, T.-W. Lee, S. K. Gray, R. G. Nuzzo, and J. A. Rogers, "Quantitative multispectral biosensing and 1D imaging using quasi-3D plasmonic crystals," Proc. Natl. Acad. Sci. U. S. A. **103**(46), 17143–17148 (2006).
45. J. Yao, M. E. Stewart, J. Maria, T.-W. Lee, S. K. Gray, J. A. Rogers, and R. G. Nuzzo, "Seeing molecules by eye: surface plasmon resonance imaging at visible wavelengths with high spatial resolution and submonolayer sensitivity," Angew. Chem. Int. Ed. **47**(27), 5013–5017 (2008).
46. X.-M. Zhao, Y. Xia, and G. M. Whitesides, "Soft lithographic methods for nano-fabrication," J. Mater. Chem. **7**(7), 1069–1074 (1997).
47. J. A. Rogers and R. G. Nuzzo, "Recent progress in soft lithography," Materials Today **8**(2), 50–56 (2005).
48. N. Kooy, K. Mohamed, L. T. Pin, and O. S. Guan, "A review of roll-to-roll nanoimprint lithography," Nanoscale Res. Lett. **9**(1), 320 (2014).
49. E. D. Palik, *Handbook of Optical Constants of Solids* (Academic, 1985).
50. A. J. Haes and R. P. Van Duyne, "A Nanoscale optical biosensor: sensitivity and selectivity of an approach based on the localized surface plasmon resonance sectroscopy of triangular silver nanoparticles," J. Am. Chem. Soc. **124**(35), 10596–10604 (2002).
51. M. D. Malinsky, K. L. Kelly, G. C. Schatz, and R. P. Van Duyne, "Chain length dependence and sensing capabilities of the localized surface plasmon resonance of silver nanoparticles chemically modified with alkanethiol self-assembled monolayers," J. Am. Chem. Soc. **123**, 1471–1482 (2001).
52. G. T. Hermanson, *Bioconjugate Techniques* (Academic, 1996).
53. L. Guo, G. Chen, and D.-H. Kim, "Three-dimensionally assembled gold nanostructures for plasmonic biosensors," Anal. Chem. **82**(12), 5147–5153 (2010).

1. Introduction

The detection and quantification of minute concentrations of biological compounds is of profound interest in diagnostic methods. While a binary detection, *i.e.* target analyte is present in the tested sample above the limit of detection, suffices in some applications others require its quantification. For example, some biological agents in our body can indicate an early stage of a disease development, such as the prostate-specific antigen (PSA) [1], the ovarian cancer cell line CA-125 [2], exosomes (microvesicles secreted by cells) [3, 4], or antibodies (present in our body as an immune system reaction against invasive antigens) [5].

Traditional labeled methods to detect biomarkers at low concentrations are the enzyme-linked immunosorbent assay (ELISA), Western blot, radioimmunoassay or those employing flourogenic or electroluminescent labels [6]. Nevertheless, these techniques are costly, time consuming and require specialized equipment and large amount of analyte. An alternative biosensing technique is the use of localized surface plasmon (LSP) supported by 2D array of subwavelength metallic scatterers, which offers multiple attractive advantages over traditional methods, for example the capability of free space optical interrogation, label free detection, real-time monitoring, small sample volume and multiplexing scalability [7, 8]. At the LSP resonance (LSPR) wavelength the local electron charge oscillation on the metal-dielectric interface induces strong field localization over subwavelength volumes. In addition, the LSPR is very sensitive to minute environmental fluctuations induced by the change in the local refractive index. An increase in the local refractive index leads to a decrease in the effective restoring force of the electron oscillations due to accumulation of polarization charges inducing a redshift in the LSPR [9].

In biological sensing applications, any biomolecule with finite optical density can trigger a measurable LSPR shift that can be quantified by optical spectroscopic techniques. Nevertheless, such inherent blindness is overcome by imposing the appropriate analyte-specific surface functionalization, *i.e.*, the target analyte is selectively immobilized on the plasmonic sensor's surface

Optics EXPRESS

through the strong surfactant-analyte binding affinity. As a result, this refractometric sensing method turns into a powerful biological detection mechanism. A large variety of biomolecules of great medical interest have been selectively detected primarily on LSPR shift employing the corresponding analyte-specific surface functionalization scheme, such as cancer biomarkers [3, 10–13] hepatitis antigens [14, 15], Alzheimer biomarker [16, 17], glucose [18–20], DNA strands [21] and proteins [22–24].

The majority of such LSP based biosensors are constructed by periodic two-dimensional arrays of isolated metallic nanoparticles or perforated holes on a continuous metallic film. They are typically fabricated using top-down techniques, such as electron-beam lithography [25, 26], focused-ion beam lithography [27, 28], nanosphere lithography [29] or hole-mask colloidal lithography [30, 31]. In one hand, electron-beam and focused-ion beam lithography are very expensive, time consuming and offer low device throughput typically over 100 x 100 ^{2} pattern area. On the other hand, the nanosphere and hole-mask colloidal lithography are cost effective but lack reproducibility in the self-assembling process over large surface area; however, not limited to a single geometrical shape [31]. In general, LSP sensors based on resonance wavelength shift suffer from low bulk figure of merits ($FoM_B = (d\lambda_{LSPR}/dn)/fwhm$, where λ_{LSPR} is the LSPR wavelength, n the environment refractive index and $fwhm$ is the resonance linewidth) due to the natural linewidth broadening of the LSPR. Such inhomogeneous linewidth broadening is inherent to these methods due to the intrinsic material losses, fabrication inhomogeneity and pattern size variation [32,33]. Coupling the plasmonic system to narrow linewidth resonances is an alternative approach to enhance the sensor's performance by narrowing the hybrid LSPR linewidth (*i.e.* higher FoM_B). For example, plasmonic systems coupled to a photonic cavity can dramatically enhance the LSP performance as demonstrated in our previous works [34, 35] or when coupled to hybrid systems exhibiting Fano-type resonances [36] or Wood's anomalies [37, 38]. In the cavity-coupled geometry the broad LSP mode couples to the narrow Fabry-Perot cavity mode when the cavity thickness is properly tuned [34, 35]. It was experimentally shown that the FoM_B of a cavity-coupled plasmonic refractometric sensor can be enhanced when compared to its uncoupled counterpart [39, 40]. However, in biosensing applications the surface sensitivity and selectivity are of paramount importance [41, 42] in order to detect the specific analyte in small concentrations, both of which were not previously addressed in similar hybrid plasmonic systems [35, 39, 40].

In this work, we demonstrate a versatile hybrid cavity-coupled plasmonic sensors as a practical biosensing platform, which was not addressed in previous plasmonic sensing approaches [35, 39, 40, 43–45]. We employed the soft nanoimprint lithography (SNIL) technique to produce high quality and reproducible biosensing substrates. This versatile nanofabrication technique enables cost effective mass scale replication of any arbitrary 2D and quasi-3D sensor design with high spatial resolution (~ 30 nm), over large area on planar or curved surfaces without the need for further post processing [46–48]. A comprehensive experimental study is carried out to assess the surface sensing property of this hybrid system using high quality conformal atomic layer depositions, which is accurately supported by full-vectorial numerical predictions. Finally, in order to demonstrate its versatility, the device is flexibly functionalized to accurately detect two very dissimilar analytes, inorganic iron oxide nanoparticle (IONP) and organic streptavidin (avidin) protein with femto to nanomolar concentrations. While the detection selectivity is imposed by the surface functionalization, the sensitivity is improved due to the narrowband hybrid plasmonic resonance on this proposed system compared to traditional nanoparticle-based plasmonic biosensors.The nanoimprinted surfaces with locked-in dimensions in the proposed work eliminates optical response uncertainties encountered in other plasmonic sensing approaches [35, 43–45]. We foresee that these highly versatile and selective cavity-coupled hybrid plasmonic systems, in conjunction with the large area SNIL technique, promises low cost biosensor development for the detection of a wide range of biomolecules of

Optics EXPRESS

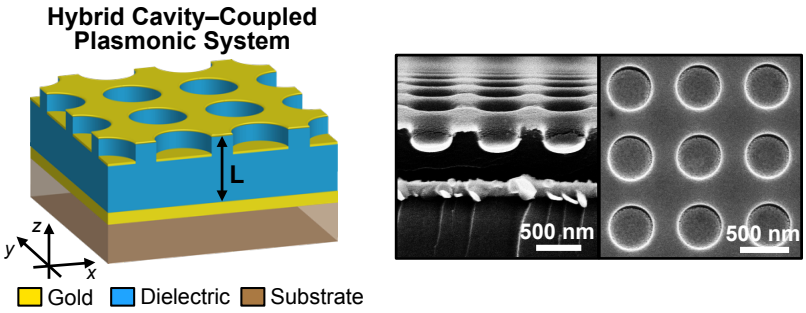

Fig. 1. Schematic representation of the hybrid cavity-coupled plasmonic system and SEM image of one fabricated device.

medical and scientific interests.

2. Optical performance

2.1. The hybrid cavity-coupled plasmonic system

The hybrid system is comprised of a semi-opaque quasi-3D plasmonic crystal, a dielectric layer and an optically thick back reflector. The devices were fabricated on 2.5x2.5 cm^2 clean glass slides thoroughly cleaned by rinsing acetone, isopropanol and DI water. An optically thick film of gold (100 nm) was evaporated, after a thin film of chromium (3 nm), using electron beam evaporation. Then, an epoxy negative photoresist (SU-8 2000.5, MicroChem Corp.) was spin casted at 3000 rpm for 30 s, prebaked at 95 C for one minute before imprinting the large-area (4x4 mm^2) square array of holes (740 nm period, 480 nm diameter and 400 nm relief depth). Each sensor was UV exposed (365 nm) for one minute following one minute post bake at 95 C. Finally, a thin film of gold (30 nm) was evaporated using electron beam to complete the device. Figure 1(a) shows the schematic representation of an ideal device and the scanning electron microscope (SEM) image of top and cross sectional views of the fabricated device.

The optical performance of the uncoupled and coupled plasmonic system is numerically studied using the finite difference time domain (FDTD) method (commercial package Lumerical Inc.). The model used in the simulations was designed according to the actual fabricated device, see inset in Fig. 2(a) for a cross section view of the model. The refractive indices for the dielectric film (SU-8 2000.5) is 1.56. The gold dispersion was fitted to experimental data [49] using a two-pole Lorentzian Drude model. The simulation volume consisted of a symmetric unit cell of 740 nm with periodic boundary conditions in the x and y directions and perfectly matched layers in the z direction. The excitation polarization was in the x direction at normal angle of incidence. Metal discontinuity of 110 nm between top film and bottom disc was used to account for the real fabricated device and evaporating condition using electron beam evaporation. Refinement meshes were employed as follows: fixed 4 nm mesh in the x and y directions on the whole simulation unit cell and for the z direction 4 nm in the top gold film and bottom gold disc and 5 nm in the well section. The cross section field monitor was placed in the xz plane at $y = 0$ and the top view field monitor was placed in the xy plance 5 nm above the top gold film.

The uncoupled plasmonic system supports a weak LSPR at $\lambda = 835$ nm as seen in the top (5 nm above the surface) and cross-sectional (center of the unit cell) electric field intensity profiles shown in Fig. 2(b). The LSPR linewidth of such uncoupled plasmonic system, as observed in Fig. 2(d) (green curve), has a complex broad resonance linewidth of approximate 200 nm full width at half maximum ($fwhm$). The LSP mode can be strongly excited by tuning the cavity thickness, which allows the Fabry-Perot resonant mode to couple with the broad LSP

Optics EXPRESS

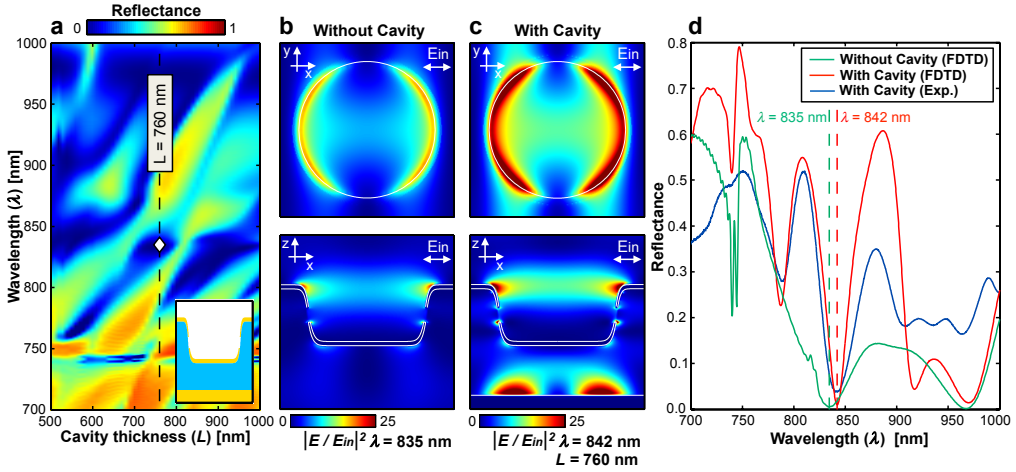

Fig. 2. (a) Calculated FDTD reflectance dispersion of the hybrid cavity-coupled plasmonic system as a function of cavity thickness (L). Inset represents the cross section profile of the simulated model. (b) Top and cross sectional spatial field profiles for a plasmonic device without cavity coupling at λ = 835 nm. (c) Top and cross sectional spatial field profiles for a plasmonic device with cavity coupling at L = 760 nm and λ = 842 nm. (d) FDTD calculated reflectance spectra of an uncoupled plasmonic system (green) and the hybrid system (red), which show a LSPR at λ = 835 nm and λ = 842 nm, respectively. Reflectance spectra comparison between experimentally measured (blue) and FDTD predicted reflectance spectra (red) for L = 760 nm.

mode forming a hybrid narrow photonic-plasmonic mode as previously demonstrated in our earlier works [34, 35]. Figure 2(a) shows the FDTD predicted reflection spectra of the hybrid system showing the complex resonance dispersion as a function of the cavity thickness (L). The normalized top and cross-sectional electric field intensity profiles, for L = 760 nm and λ = 842 nm, are plotted in Fig. 2(c). The local field enhancement is considerably stronger (two times) and narrow band in the coupled system ($fwhm$ ~26.2 nm) than its uncoupled counterpart ($fwhm$ ~200 nm) for the same plasmonic mode but slightly redshifted from λ = 835 nm to λ = 842 nm. Compared to the uncoupled plasmonic system, the hybrid LSP mode is ~87% narrower and well defined as can be seen in Fig. 2(d), which shows the effect of the optical cavity in further reducing the LSPR linewidth as well as enhancement of the local near-field strength. Both local field enhancement and sharp narrowband resonance is beneficial in order to achieve a high figure of merit when such system is used for sensing applications. A strong local field enhances light-matter interaction with the target molecule whereas sharp narrowband resonance improves detectability. Contrary to LSP gap modes in nanoparticle or nanorod dimers where strong field enhancement over subwavelength volume are not easily accessible, the proposed architecture allows the cavity-enhanced LSP near field located on the exposed sensor's surface to be in direct contact with the target analyte for high sensitive detection.

The sensor characterization is based on unpolarized reflectance spectroscopy using a microscope-coupled Fourier transform infrared spectrometer in the NIR domain (Hyperion 1000 - Vertex 80, Bruker Inc.). Gold mirror was used as the background reference. A tungsten filament source, CaF_2 beam splitter and objective lens (0.07 NA) and Si detector were used to perform the reflectance measurement in the NIR band (700-1000 nm). An aperture of 2.5 mm in diameter focused the light beam onto a spot of ~0.8 mm in diameter and the excitation was carried out at normal incidence. The reflection spectrum of a fabricated device is compared in Fig. 2(d) with the FDTD predicted spectrum at a cavity thickness L = 760 nm with excellent

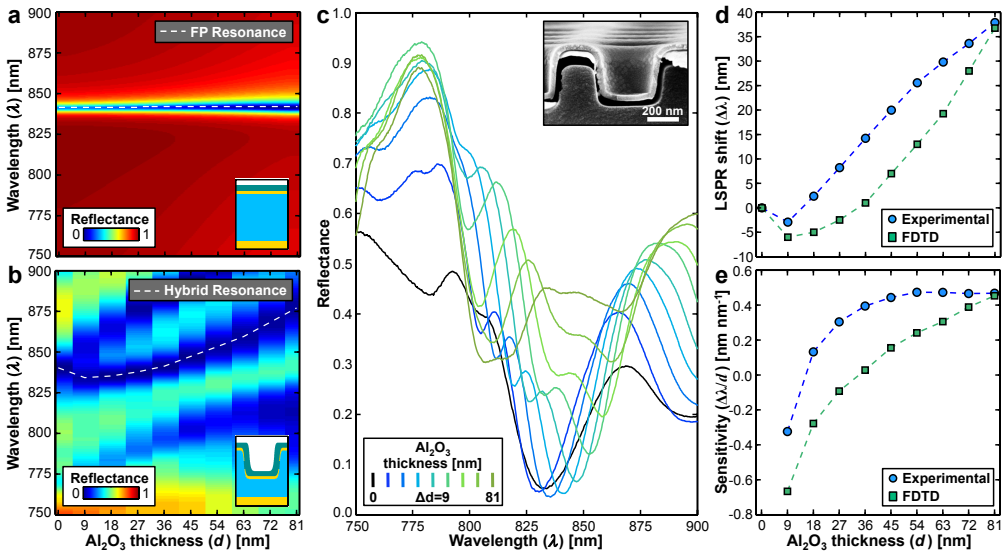

Fig. 3. (a) Theoretical reflectance of a multistack showing a Fabry-Perot resonance (white dashed line) independent of the Al_2O_3 thickness (d). The multistack is comprised of air superstrate, Al_2O_3 film (0-81 nm), gold thin film (30 nm), SU8 as a dielectric (760 nm) and gold back reflector (200 nm). (b) FDTD reflectance dispersion of a hybrid cavity-coupled plasmonic system as a function of Al_2O_3 thickness showing the hybrid resonance dispersion (white dashed line). (c) Experimental reflectance of the hybrid cavity-coupled plasmonic system as a function of Al_2O_3 conformal layers at different thicknesses. The inset SEM image corresponds to a coated device with 36 nm Al_2O_3. (d) Experimental (blue circles) and FDTD (green squares) LSPR shift as a function of Al_2O_3 thickness. (e) Experimental (blue circles) and FDTD (green squares) surface sensitivity as a function of Al_2O_3 thickness.

spectral correlation.

2.2. *Surface sensing performance*

As theoretically demonstrated in a multi-layer stack comprising of an asymmetric Fabry-Perot resonator with a thin film of aluminum oxide (Al_2O_3) with refractive index of 1.759 (inset of Fig. 3(a)), the photonic resonance does not experience dispersion with respect to thickness variation of a test Al_2O_3 film less than 100 nm as seen in Fig. 3(a). On the contrary, the LSP mode generates near-field that extends in the vicinity of the metallic surface, as observed in Fig. 2(c), where any molecule placed within that volume contributes to the spectral shift of the LSPR [41, 42]. For example, same Al_2O_3 film test on the cavity-coupled plasmonic system at L = 760 nm shows clear LSPR shift with respect of film thickness, see Fig. 3(b).

In order to experimentally study the surface sensitivity of this device we used the atomic layer deposition (ALD) technique to coat nine high quality conformal layer of Al_2O_3 with atomic layer precision using the Savannah system. Studying the LSPR behavior upon controlled conformal layer deposition provides insights into the surface-sensing abilities of the hybrid LSPR system. FDTD calculations of Al_2O_3 thin film coating were performed to better understand the experimental observations. For the accurate track of the Al_2O_3 effect on the LSPR additional refinement meshes were added with the same x and y resolution as before (4 nm) but with 3 nm resolution in z. First of all, this study gives an estimate of the maximum conformal layer thickness that can be measured without detuning the plasmonic hybrid mode away from the photonic resonance. This spectral bandwidth defines the overall dynamic range of the sensor. Secondly,

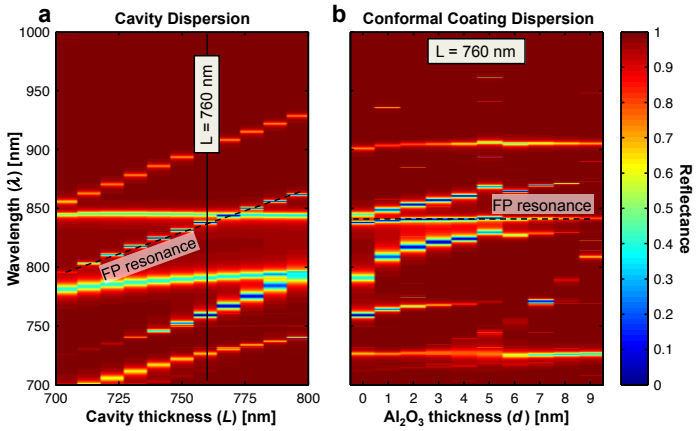

Fig. 4. Reflection spectra of a hybrid system with perfect electrical conductor (PEC) interchanging the top gold film. (a) Reflection spectra dispersion as a function of cavity thickness. This graph shows a Fabry-Perot (FP) resonance (dashed line). (b) Reflection spectra dispersion as a function of conformal coating film thickness that shows no dispersion of a FP resonance at $L = 760$ nm.

the conformal inorganic material (Al_2O_3) growth on the nanostructured surface functions as a test for the actual biomolecular thin-film coating.

The surface sensitivity is experimentally studied by depositing high quality conformal Al_2O_3 films in 9 nm increments, from 0 to 81 nm. The reflection spectra were measured after each 9 nm cycle of Al_2O_3 film growth. The measured reflection spectra are plotted in Fig. 3(c). The LSPR wavelength shift with respect to the bare uncoated case as a function of Al_2O_3 layer thickness (d) are plotted in Fig. 3(d) along with the corresponding FDTD predictions. A dynamic range of 40 nm was estimated for an Al_2O_3 thickness of 80 nm before the cavity gets detuned. FDTD calculations show similar trend of the LSPR dispersion as a function of Al_2O_3 as observed in Figs. 3(b) and 3(d). The surface sensitivity of the system is defined as $S = \Delta\lambda/d$ [42], where $\Delta\lambda$ is the LSPR spectral shift and d is the deposited film thickness. Figure 3(e) shows the spectral sensitivity as a function of Al_2O_3 thickness along with the corresponding FDTD predicted spectral sensitivity. As observed, both experimentally and numerically, the LSPR blueshifts after the first film deposition and then steadily redshifts until the LSPR decouples from the cavity mode and reappears at a shorter wavelength. This initial blueshift arises from the influence of the gap formed between the top-hole and bottom-disc as observed in our simulations (not included here) when it changes from air to a denser media (Al_2O_3). As the initial Al_2O_3 layer is grown on the system, the LSPR mode at $\lambda = 830$ nm experiences an extra phase on top of the original cavity phase, modifying the total round-trip phase. Subsequently, the coupled LSPR redshifts after each Al_2O_3 layer deposition until completely detunes away from the photonic cavity. At that point, the coupled LSPR mode weakens substantially and another spectral feature appears in the 800 nm range, as observed in Fig. 3(c). Such spectral shift and cavity detuning is the signature of the LSP-cavity interaction because in a system that does not support LSP modes, for example when the top gold film is interchanged by a perfect electrical conductor (PEC), the supported FP modes do not experience dispersion as a function of thin conformal Al_2O_3 layers as seen Fig. 4.

3. Biosensing

The surface sensing performance of this hybrid system is further explored in two sensing experiments to detect inorganic amine-coated iron oxide nanoparticles (A-IONP) and organic

Optics EXPRESS

avidin protein. Detection of inorganic nanoparticles, through the organic amine coating, is of great interest due to their ability to amplify the LSP signal when conjugated with other, low mass, analytes [24, 50]. On the other hand, biotin-avidin model stands as an efficient biological model to test biosensing devices because of their strong binding affinity (10^{-14} mol/L). In addition, the strong biotin-avidin binding affinity is efficiently exploited in various antibody-antigen detection schemes [6, 13, 15, 50]. The corresponding chemical surface functionalization schemes were employed for analyte-specific binding. In order to ensure that the whole sensor's surface is active towards the target analyte, we optimized the incubation time to maximize surface functionalization [51]. The hybrid system, after chemical surface functionalization captures the target analyte through high affinity binding which results in a LSPR spectral shift. The spectral measurements were performed in a dry environment. In all cases the reflection spectra were measured to obtain the corresponding LSPR resonance shift with respect to the bare sensor (λ_0) after adding the target analyte (λ_a). The actual spectral shift ($\Delta\lambda = \lambda_a - \lambda_0$) is determined as the LSPR shift between the bare sensor resonance and the analyte-binding step. The biosensor characterization was performed in a batch of devices, one for avidin and another for A-IONPs equally functionalized with the corresponding surfactant, and then each sensor was subject to a determined analyte concentration.

3.1. Materials and synthesis.

3.1.1. Materials

(+)-α-Lipoic Acid (LA), 1,4-Dithio-DL-threitol (DTT), 1-Ethyl-3-(3-dimethylaminopropyl) carbodiimide (EDC), N-Hydroxy-succinimide (NHS), streptavidin, bovine serum albumin (BSA), $FeCl_3.6H_2O$, $FeCl_2.4H_2O$, NH_4OH, hydrogen chloride (HCL), N,N'-Dicyclohexylcarbodiimide, tetrahydrofuran, ethyl acetate, hexane, poly(acrylic acid), pyridine, dimethylformamide, Biotin-PEG_{11}-NH_2, were used as received. Lipoic Acid conjugates were synthesized using NHS chemistry.

3.1.2. Iron oxide nanoparticle synthesis.

An iron solution consisting of $FeCl_3.6H_2O$ (0.62 g), $FeCl_2.4H_2O$ (0.32 g), H_2O (2 mL) and HCl (100 L) was added to a 12% (v/v) aqueous solution of NH_4OH under mild mixing. The solution was allowed to mix for 30 seconds to allow for nucleation. Then poly(acrylic acid) (820 g) was dissolved in H_2O (15 mL) and added to the iron solution under rigorous mixing for one hour. The iron oxide nanoparticles (IONP) were purified via centrifugation (30 minutes, 4,000 rpm, three times) to remove large iron particles and with a KROS FLO filter (Spectrum Labs) to remove excess ammonium hydroxide. The nanoparticles size (80-100 nm) was determined by dynamic light scattering (Zetasizer Nano ZS, Malvern).

3.1.3. Lipoic acid-NHS synthesis.

N,N'-Dicyclohexylcarbodiimide (6.00 g) was dissolved in tetrahydrofuran (10 ml) and added slowly to a LA solution (5.00 g) and NHS (3.35 g) in tetrahydrofuran (150 ml) at 40 °C. The mixture was warmed to room temperature and stirred for 5 hours. The precipitate was removed by vacuum filtration and the solvent evaporated *in vacuo*. The crude product was re-dissolved in ethyl acetate (100 ml) and filtered once more by vacuum filtration. The product was recrystallized from a solution of hot ethyl acetate/hexane (1:1 v/v) as a pale yellow solid (5.88 g, 80%). [1H NMR (400MHz, $CDCl_3$): ä(ppm) 3.58 (m,1H), 3.13 (m, 2H), 2.84 (s, 4H), 2.63 ((t, J)7.1 Hz, 2H), 2.50 (m, 1H), 1.99-1.46 (m, 7H)].

3.1.4. Lipoic acid-PEG11-biotin synthesis.

Biotin-PEG_{11}-NH_2 (50 mg) and catalytic amounts of pyridine (10 L) were added to Lipoic Acid-NHS (18.71 mg) in dry dimethylformamide (DMF) (2 ml). The mixture was stirred overnight

Optics EXPRESS

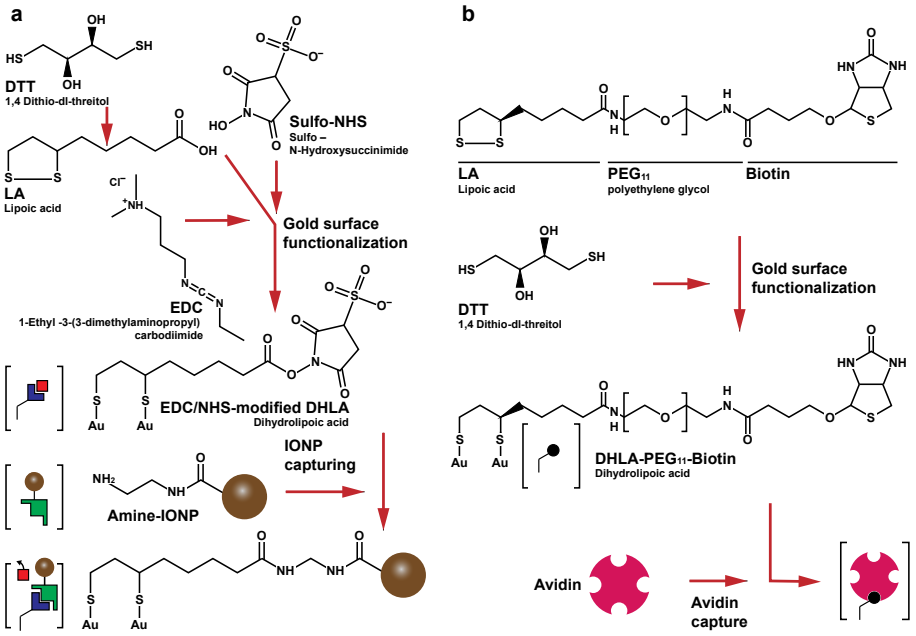

Fig. 5. Gold surface functionalization and detection schemes for selective analyte detection. (a) Amine-coated IONP binding. LA is bound to the gold surface by reduction of its sulfur bond through DTT. EDC/NHS chemistry activates the DHLA terminal group to bind amine-coated IONP. (b) Avidin binding. The synthetized LA-PEG_{11}-Biotin is bound to the gold surface by reduction of its sulfur bond through DTT. Streptavidin binds directly to biotin with high affinity.

at room temperature. The reaction mixture was then dried *in vacuo* and the resulting solid was re-dissolved in water to precipitate unreacted LA-NHS. The mixture was centrifuged and the supernatant was collected. The product was lyophilized and resulted in thick yellow oil.

3.2. Iron oxide nanoparticle detection.

A-IONPs were selectively bound to the gold surface using lipoic acid (LA) and EDC/NHS [52] functionalization chemistry. Each device was washed with deionized water and allowed to dry prior to being submerged in LA (5 mL of 10 mM) and DTT (5 mL of 10 mM) in pure ethanol. LA reduction allow the thiol groups to bind to the gold surface. The sensors were incubated overnight at room temperature, and then washed twice with pure ethanol to remove any unreacted Dihydrolipoic Acid (DHLA) or DTT. The resulting dihydrolipoic acid (DHLA) coated sensors were activated using different concentrations of EDC and NHS (1:1 ratio, from 1 fM to 100 M) to activate the DHLA binding sites and subsequently let A-IONPs capturing through a strong amide linkage. A fixed concentration of A-IONP (0.05 mg/mL) in a total volume of 10 mL H_2O was added and allowed to react with the sensor for 15 hrs. The sensors were then washed three times with DI water in order to remove any unreacted or excess material. This chemical workflow is depicted in Fig. 5(a). Contrary to the conventional binding methods where the entire surface is saturated with the surfactant, which determines the concentration of the analyte that can bind to it, in this method the DHLA-functionalized surface is activated to bind only a maximum concentration of analyte dictated by the EDC/NHS activating concentration. The graphical representation of the binding process is depicted in Fig. 6(a). In Fig. 6(b) the average LSPR spectral shift (red square marks) is plotted as a function of A-IONP concentration showing

Optics EXPRESS

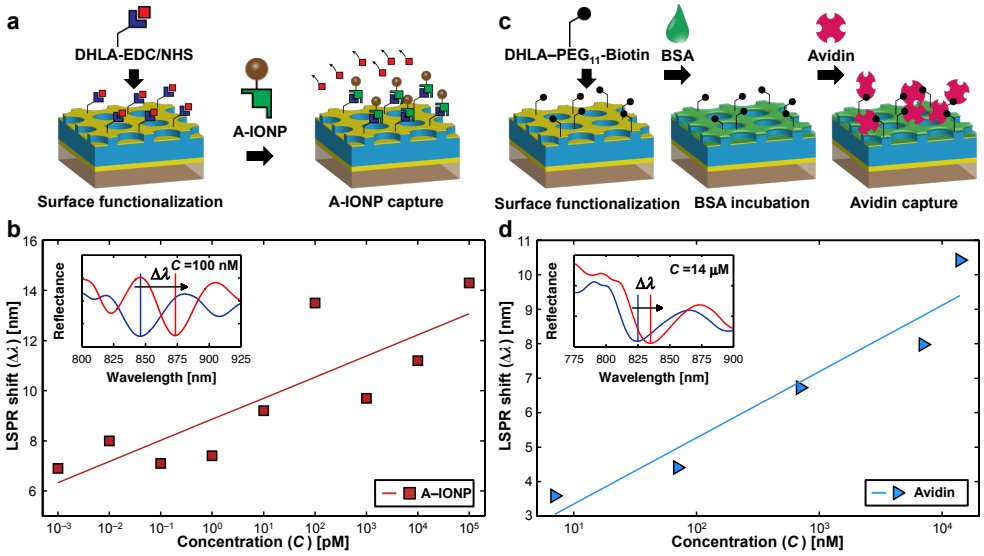

Fig. 6. (a) Schematic representation of A-IONP capturing. DHLA-EDC/NHS surface functionalization and A-IONP capture through amine-NHS interchange. (b) Average LSPR spectral shift of A-IONP with respect to DHLA activated with different concentrations (C) of EDC/NHS chemistry. Continuous line represents logarithmic fit ($R^2 = 0.70$) to the experimental data. Inset shows the LSPR shift response from the un-functionalized sensor (blue curve) to a concentration of $C = 100$ nM (red curve). (c) Schematic representation of Avidin capturing through sensor's Biotin functionalization and BSA surface saturation for reduction of nonspecific binding. (d) Average LSPR spectral shift with respect of Avidin concentration (C). Continuous lines represent logarithmic fit ($R^2 = 0.92$) to the experimental data. Inset shows the LSPR shift response of an un-functionalized sensor (blue curve) to a concentration of $C = 14$ M (red curve).

a logarithmic trend ($R^2 = 0.70$) in LSPR shift represented by the continuous line. A femto molar concentration was reliably detected with ~6 nm minimum spectral shift.

3.3. *Avidin detection.*

As a next step the device was employed to detect avidin protein. Each device was washed with deionized water and allowed to dry prior to being treated with lipoic acid - polyethelene glycol - biotin (LA-PEG_{11}-Biotin) (20 L of 10 mM) and DTT (20 L of 10 mM) in DI water to break the sulfur bond in order to facilitate binding to the gold surface. The sensors were incubated for three hours at room temperature, and then washed three times with DI water to remove any unreacted DHLA-PEG_{11}-Biotin or DTT. The devices were incubated in BSA (2 mM) for three hours and washed three times with DI water prior to the addition of streptavidin (40 L) at different concentrations (7 nM to 14 M, 1% BSA (v/v)). The sensors were incubated three hours and then washed three times with DI water. The chemical formulation for this experiment is shown in Figs. 5(b) and 6(c) schematically illustrates the binding process. The corresponding average LSPR shift is plotted in Fig. 6(d), which shows a logarithmic response fit ($R^2 = 0.92$) represented by the continuous line, as a function of avidin concentration. In order to reduce non-specific binding the sensor's surface was saturated with BSA right after the biotin functionalization step. In addition, BSA surface passivation improved detection accuracy by reducing the spread of the measured data compared to the A-IONPs detection (Fig. 6(b)). Nanomolar concentration of avidin was achieved resulting in ~3 nm LSPR shift.

Optics EXPRESS

Different plasmonic biosensors, following conventional top-down, bottom-up or a combination of them have been reported with limit of detection in the nano to picomolar range. For example, Aćimović *et al.* showed, in a microfluidic integrated with gold nanorods, an avidin detection limit of 0.32 nM [13]. Amanda *et al.* used silver nanotriangles and obtained a limit of detection in the low-picomolar concentration without amplification [50]. Guo *et al.* employed gold nanoparticles and multi-walled carbon nanotubes to construct a three-dimensional scaffold working as a biosensor and obtained 0.5 nM detection [53]. Here, in A-IONPs and avidin detection, a femto and nanomolar concentrations were reliably detected with 6 nm and 3 nm spectral shift, respectively, which promises further improvement in limit of detection considering sub-nanometer detection resolution of present spectrometers. These two sensing experiments provide evidence of the robust and versatile biosensing capability of this hybrid plasmonic system with similar range of previously reported low limit of detection. The biotin-avidin lock-key mechanism facilitates detection of a wide range of protein and other bio-molecules. Further detection of inorganic materials, such as IONPs or other metallic nanoparticles, is well suited as amplifying agents of low mass molecules as previously reported [50, 53].

4. Conclusions

Biosensing application of plasmonic systems is an active field of interest that has attracted scientists from different backgrounds. However, the selective detection of biological material in a simple way with cheap substrates has remained elusive over decades. While the selective detection has been proven since the 90's and numerous biomarkers, viruses and proteins have been detected using LSP-based biosensors, the transfer from fundamental research to practical applications is still challenging. This limitation is mainly due to the inherent low performance of plasmonic devices and fabrication challenges. In this work we showed that the cavity-coupled plasmonic sensors have excellent surface sensing performance under controlled surface functionalization, which is of great importance in biosensing. We demonstrated selective detection of two very dissimilar analytes, iron oxide nanoparticles (inorganic) and avidin protein (organic), under very low concentration. In addition, such hybrid-plsmonic substrates can be used in conjunction with Raman spectroscopy for enhanced blind identification of bio-molecules based on unique molecular spectral fingerprints. The expansion to other analytes can be straightforward implemented by imposing the corresponding surface functionalization scheme. Further work is expected in direct detection of a specific analyte from a bath of several analytes such as in biological fluids, for example human plasma, serum, urine, saliva, tear or sweat. We foresee that these hybrid cavity-coupled plasmonic systems in conjunction with the simple low cost nanoimprinting technique will pave the path towards robust plasmonic biosensors for low-concentration and label-free detection of biomolecules.

Funding

NSTC/UCF start-up. Florida Space Institute/NASA (63019022). NSF-EEC (1156747). CONACyT (PhD Fellowship).

Acknowledgment

A.V.G. acknowledges support from the National Council of Science and Technology (CONACyT), the Secretariat of Public Education (SEP) and the Mexican Government. J.O. acknowledges support from the UCF-REU program for "Hard and Soft Materials in Nanoscience Technology Driven Energy Applications".